Competition between roll and square convection patterns in binary mixtures

H. W. Müller and M. Lücke

Institut für Theoretische Physik, Universität des Saarlandes, D-6600 Saarbrücken, West Germany

(Received 28 March 1988)

We present a few-mode Galerkin model for convection in binary fluid layers subject to impermeable horizontal boundary conditions at positive separation ratios. It describes convection in the form of rolls in x direction, y direction, and squares. To incorporate symmetry-breaking sidewall forces selecting the spatial phase of the patterns relative to the walls we introduce into the model equations a single small inhomogeneity that favors the experimentally realized phase. Then squares are stabilized shortly above onset of convection where the amplitudes are very small. Far above onset, the amplitudes strongly increase, nonlinear mode coupling dominates, and causes rolls to be stable. In an intermediate regime, there are oscillations between the three competing patterns of rolls in x direction, squares, and rolls in y direction. Heat transport, spatial, and temporal behavior of the various convective states are in good agreement with recent experiments.

I. INTRODUCTION

Already close to the threshold for onset of convection in a binary fluid layer heated from below[1] the interplay between currents of momentum, heat, and concentration leads to rich and interesting linear and nonlinear behavior.[2-8] The convective momentum currents are driven by buoyancy forces that result from vertical mass density variations due to temperature and concentration gradients. These two driving mechanisms can be controlled externally by varying the Rayleigh number R, i.e., the temperature stress and the separation ratio ψ (Ref. 9) which measures the concentration driving:[8] $\psi > 0$ implies concentration gradients such that convective currents are enhanced, while the opposite holds for $\psi < 0$.

Recently, Moses and Steinberg[6] (MS) examined convection patterns and heat transport in ethanol water mixtures at small positive separation ratios $0.01 \lesssim \psi \lesssim 0.1$. Their heat transport measurements showed two distinct ranges in the plot Nusselt number N, i.e., reduced heat transport, versus Rayleigh number. For slightly supercritical R the Nusselt number and its slope are very small and the convective motion is driven by the solute gradient via the Soret effect.[1,10] MS defined this range of almost vanishing convective heat transport as the Soret regime. For larger Rayleigh numbers the slope of N sharply increases to a higher value which is close to the slope for convection in a pure fluid. This second range is defined as the Rayleigh regime.

MS found stationary square convective patterns within the Soret regime and stationary roll patterns in the far Rayleigh regime. In a region of Rayleigh numbers between these two regimes they observed in square experimental cells (and also in cylindrical containers) *periodically alternating* patterns of squares and rolls. Le Gal et al.[11] did similar experiments to those of MS in circular cells. However, they used oil, i.e., a multicomponent fluid instead of a pure binary mixture. They also found at small Rayleigh numbers stationary square convective patterns, then oscillating patterns of squares and rolls, and

then for still larger R stationary roll patterns.

In this work we present a model that is able to reproduce and to explain the main features of the experiments of MS. We shall see that the stationary square patterns at onset of convection just as the oscillating square and roll patterns at slightly larger Rayleigh numbers are a genuine phenomenon of binary mixtures with positive separation ratios.

In Sec. II we introduce a low-mode Galerkin model for binary mixtures between impermeable horizontal boundaries. In Sec. III we investigate its stationary solutions describing square and roll convection and its oscillatory solutions describing alternating patterns of squares and rolls. In Sec. IV we discuss the fact that sidewall forces in the experimental cell select particular spatial phases of the convective patterns. We incorporate such forces phenomenologically into our model, we determine their effect on linear and nonlinear properties of the stationary and oscillatory convective states, and we compare with experiments. Section V contains a summary of our results.

II. GALERKIN MODEL

Consider a layer of a binary fluid mixture extending laterally, i.e., in the x-y direction to infinity and heated from below. Neglecting the Dufour effect[1,10] the nondimensionalized equations of motion for the deviations from the conductive state read in Oberbeck-Boussinesq approximation[1,10]

$$\nabla \cdot \mathbf{u} = 0 , \tag{2.1a}$$

$$(\partial_t + \mathbf{u} \cdot \nabla)\mathbf{u} = -\nabla p + \sigma[(1+\psi)\theta + \zeta]\mathbf{e}_z + \sigma \nabla^2 \mathbf{u} , \tag{2.1b}$$

$$(\partial_t + \mathbf{u} \cdot \nabla)\zeta = L \nabla^2 \zeta - \psi \nabla^2 \theta , \tag{2.1c}$$

$$(\partial_t + \mathbf{u} \cdot \nabla)\theta = R u_3 + \nabla^2 \theta . \tag{2.1d}$$

The vector $\mathbf{u}(\mathbf{x}, t)$ is the velocity field, $p(\mathbf{x}, t)$ the pressure, and $\theta(\mathbf{x}, t)$ the temperature. The combined field

$$\zeta(\mathbf{x}, t) = c(\mathbf{x}, t) - \psi \theta(\mathbf{x}, t) \tag{2.2}$$

is used instead of the concentration field $c(\mathbf{x},t)$. Then the impermeability of the horizontal boundaries to concentration currents can be imposed in a mathematically more convenient way. Lengths are scaled by the layer thickness d, multiplied by the vertical diffusion time d^2/κ where κ is the thermal diffusivity. We have scaled temperatures by $\nu\kappa/\beta_1 g d^3$ and concentration by $\nu\kappa/\beta_2 g d^3$ where ν is the kinematic viscosity, g the gravitational constant, and β_1 (β_2) the thermal (solutal) expansion coefficient at constant concentration (temperature) and pressure. Moreover, $\sigma = \nu/\kappa$ is the Prandtl number, and the Lewis number $L = D/\kappa$ is the ratio of mass diffusivity D and thermal diffusivity κ. There are two control parameters: the separation ratio ψ and the Rayleigh number $R = \Delta T \beta_1 g d^3/\nu\kappa$ where ΔT is the externally imposed temperature difference between the upper and the lower plate at $z = 1$ and 0, respectively.

A. Selection and truncation of the modes

To describe the convective flow we use a Galerkin technique and expand the spatial dependence of the hydrodynamic fields in Fourier series appropriate to free-slip, impermeable (FSI) horizontal boundary conditions,

$$\phi(\mathbf{x},t) = \sum_{\mathbf{n}} \hat{\phi}_{\mathbf{n}}(t) e^{i\mathbf{q}(\mathbf{n})\cdot\mathbf{x}} , \qquad (2.3a)$$

with

$$\mathbf{n} = (n_1, n_2, n_3), \quad n_i = 0, \pm 1, \pm 2, \dots \qquad (2.3b)$$

$$\mathbf{q}(\mathbf{n}) = (k n_1, k n_2, \pi n_3) . \qquad (2.3c)$$

It has recently become clear that the impermeability of the horizontal boundaries significantly affects linear[8,12-14] and nonlinear[12,15] properties of binary mixtures. The reason is the additional coupling between temperature and concentration gradients at the boundaries arising from the condition that the vertical concentration current has to vanish there. We use physically unrealistic but mathematically convenient free-slip conditions on the lateral momentum currents at the horizontal boundaries. The influence of the slip condition on convection seems to be much less important.[12,16,17] It gives rise to different wave numbers, critical Rayleigh numbers, and frequencies, i.e., effects that can partly be taken care of by using properly scaled quantities.

The expansion (2.3) will be truncated so as to describe with a minimal set of modes convection in the form of straight rolls parallel to the x axis, parallel to the y axis, and convection in square form. We restrict ourselves in this work to convective patterns that do not move laterally, thus the phases of the complex amplitudes $\hat{\phi}_{\mathbf{n}}$ do not vary in time. The patterns are invariant under translation in the x and y directions by half a wavelength. Furthermore, a possible convective pattern is transformed via rotation around the z axis by integer multiples of $\pi/2$ into another possible pattern.

The selection of the modes retained in the truncation is based on the following reasoning.

(i) First we take the basic critical modes, i.e., the lowest modes that can grow above the convective threshold

within the linearized equations. The associated wave numbers in the region of reciprocal space with positive mode indices are shown in Fig. 1 by closed symbols. They are, e.g., (101) and (011) for θ and $\mathbf{u}$ and (100) and (010) for ζ. In each case the modes with $n_1 = 0$ or $n_2 = 0$ describe convective roll patterns with axes parallel to the x or y axis, respectively.

(ii) In addition, we retain the first modes that are coupled to the above basic critical modes via the nonlinear convective interactions on the left-hand side of (2.1). These modes are shown in Fig. 1 by open symbols. For example, the (112) mode of θ and $\mathbf{u}$ is driven by the combination of a (101) and a (011) mode in the nonlinearities $(\mathbf{u}\cdot\nabla)\theta$ and $(\mathbf{u}\cdot\nabla)\mathbf{u}$, respectively. On the other hand, the form of the mode interaction $(\mathbf{u}\cdot\nabla)\zeta$ appearing in (2.1c) is such that it can generate only a (001) mode in the ζ field by combining the critical modes of $\mathbf{u}$ and ζ (closed triangles and squares, respectively, in Fig. 1) but not a (111) mode. To find all these additional modes one merely has to list the triple-mode interactions of the form $\mathbf{q} + \mathbf{q}' = \mathbf{q}''$ that involve two basic critical modes. Modes which in principle are possible by this procedure but incompatible with incompressibility or thermal boundary conditions (e.g., $\hat{u}_{002}$ or $\hat{\theta}_{110}$) are discarded. The mode $\hat{u}_{110}$ turns out to be damped away.

(iii) We neglect the modes $|n_1| > 1$, $|n_2| > 1$ that represent higher lateral harmonic variations of the fields.

With the modes shown in Fig. 1 we then obtain for the vertical component of the velocity field
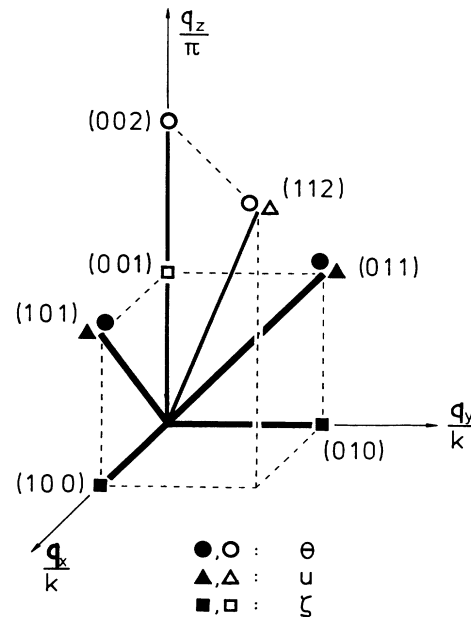

FIG. 1. Wave vectors retained in the truncation of the Fourier expansion of the hydrodynamic fields $\mathbf{u}$ (triangles), θ (circles), and ζ (squares). Shown is only one-eighth of $\mathbf{k}$ space. Closed symbols and thick lines denote the basic critical modes, while open symbols and thin lines show modes that are coupled via the convective nonlinearities to the basic modes. See text for more details.

$$u_3(\mathbf{x},t) = 2\sqrt{2}[\hat{u}_{101}(t)\cos(kx) + \hat{u}_{011}(t)\cos(ky)]\sin(\pi z)$$
$$+ 4\sqrt{2}\hat{u}_{112}(t)\cos(kx)\cos(ky)\sin(2\pi z) \ . \quad (2.4a)$$

The horizontal velocity fields u_1 and u_2 follow via the continuity equation,

$$u_1(\mathbf{x},t) = -2\sqrt{2}\frac{\pi}{k}[\hat{u}_{101}(t)\sin(kx)\cos(\pi z)$$
$$+ 2\hat{u}_{112}(t)\sin(kx)\cos(ky)\cos(2\pi z)] \ , \quad (2.4b)$$

$$u_2(\mathbf{x},t) = -2\sqrt{2}\frac{\pi}{k}[\hat{u}_{011}(t)\sin(ky)\cos(\pi z)$$
$$+ 2\hat{u}_{112}(t)\cos(kx)\sin(ky)\cos(2\pi z)] \ . \quad (2.4c)$$

For the deviation from the conductive temperature profile we get

$$\theta(\mathbf{x},t) = 2\sqrt{2}[\hat{\theta}_{101}(t)\cos(kx) + \hat{\theta}_{011}(t)\cos(ky)]\sin(\pi z)$$
$$+ \sqrt{2}[4\hat{\theta}_{112}(t)\cos(kx)\cos(ky) + \hat{\theta}_{002}(t)]\sin(2\pi z) \ , \quad (2.4d)$$

and for the combined field ζ

$$\zeta(\mathbf{x},t) = 2\hat{\zeta}_{100}(t)\cos(kx) + 2\hat{\zeta}_{010}(t)\cos(ky)$$
$$+ \sqrt{2}\hat{\zeta}_{001}(t)\cos(\pi z) \ . \quad (2.4e)$$

The expansion of the z dependence of ζ in cos modes[12] guarantees impermeability since the vertical component of the concentration current, $-L\nabla_3\zeta$, vanishes at the horizontal boundaries $z=0,1$. All mode amplitudes appearing in (2.4) are real. To arrive at (2.4) we used the reality of the fields, the constraints imposed by mirror and inversion symmetry of the patterns to be described, and the fact that the patterns are standing. Note that the relative spatial phases of the fields in (2.4) have been fixed.

If one were to discard all y-dependent (x-dependent) terms in (2.4), i.e., if one would keep only the wave vectors in the k_x-k_z (k_y-k_z) plane of Fig. 1 then one would have a five-mode truncation describing a standing pattern of convective rolls perpendicular to the x axis (y axis). Thus the fields (2.4) may be visualized by a superposition of two sets of mutually perpendicular convective rolls with weights given by the corresponding mode amplitudes. In addition, however, there appears also a lateral contribution, e.g., $\sim\cos(kx)\cos(ky)$, that is generated by the nonlinear interaction of the roll-type fields. Thus our truncation leads to a natural but nontrivial extension of the five-mode Lorenz models[18] for binary mixtures which describe standing roll patterns.

B. Model equations

Projecting the equations of motion (2.1) onto the ten modes retained in the Galerkin ansatz (2.4) we obtain the following generalized Lorenz model:

$$\tau\dot{\mathbf{X}} = -\sigma\hat{q}^2\mathbf{X} + \sigma\frac{\hat{k}^2}{\hat{q}^2}\left[(1+\psi)\mathbf{Y} + \frac{8}{\pi^2}\mathbf{U}\right] + \begin{bmatrix} X_2 \\ X_1 \end{bmatrix}S \ , \quad (2.5a)$$

$$\tau\dot{\mathbf{Y}} = -\hat{q}^2\mathbf{Y} + (r-Z)\mathbf{X} + \begin{bmatrix} X_2 \\ X_1 \end{bmatrix}T \ , \quad (2.5b)$$

$$\tau\dot{\mathbf{U}} = -\frac{L}{3}\hat{k}^2\mathbf{U} + \hat{q}^2\psi\mathbf{Y} + V\mathbf{X} \ , \quad (2.5c)$$

$$\tau\dot{Z} = -b(Z - \mathbf{X}\cdot\mathbf{Y}) \ , \quad (2.5d)$$

$$\tau\dot{V} = -b\left[\frac{L}{4}V + \tfrac{2}{3}\psi Z + \tfrac{1}{2}\mathbf{X}\cdot\mathbf{U}\right] \ , \quad (2.5e)$$

$$\tau\dot{S} = -2\sigma\hat{d}^2S + \sigma(1+\psi)\frac{\hat{k}^2}{\hat{d}^2}T - \frac{4}{3}\frac{\hat{q}^2}{\hat{d}^2}X_1X_2 \ , \quad (2.5f)$$

$$\tau\dot{T} = rS - 2\hat{d}^2T - \frac{b}{4}(X_1Y_2 + X_2Y_1) \ . \quad (2.5g)$$

Here we have combined the critical modes into two-component vectors defined by

$$\mathbf{X} = \begin{bmatrix} X_1 \\ X_2 \end{bmatrix} = \frac{1}{q_c^0}\begin{bmatrix} \hat{u}_{101} \\ \hat{u}_{011} \end{bmatrix} \ ,$$

$$\mathbf{Y} = \begin{bmatrix} Y_1 \\ Y_2 \end{bmatrix} = \frac{q_c^0}{R_c^0}\begin{bmatrix} \hat{\theta}_{101} \\ \hat{\theta}_{011} \end{bmatrix} \ , \quad (2.6a)$$

$$\mathbf{U} = \begin{bmatrix} U_1 \\ U_2 \end{bmatrix} = \frac{\pi q_c^0}{2\sqrt{2}R_c^0}\begin{bmatrix} \hat{\zeta}_{100} \\ \hat{\zeta}_{010} \end{bmatrix} \ .$$

The current-carrying modes for heat and concentration are

$$Z = -\frac{\pi\sqrt{2}}{R_c^0}\hat{\theta}_{002}, \quad V = \frac{\pi^2}{2\sqrt{2}R_c^0}\hat{\zeta}_{001} \ , \quad (2.6b)$$

and the two additional modes are

$$S = \frac{\pi\sqrt{2}}{q_c^{0^2}}\hat{u}_{112}, \quad T = \frac{\pi\sqrt{2}}{R_c^0}\hat{\theta}_{112} \ . \quad (2.6c)$$

We have used the constants

$$k_c^{0^2} = \frac{\pi^2}{2}, \quad q_c^{0^2} = k_c^{0^2} + \pi^2, \quad R_c^0 = \frac{q_c^{0^6}}{k_c^{0^2}} \ ,$$

$$\tau = \frac{1}{q_c^{0^2}}, \quad b = \frac{4\pi^2}{q_c^{0^2}} \ , \quad (2.6d)$$

which are the critical quantities of the model for $\psi = 0$. They are also used to define the following reduced quantities:

$$r = \frac{R}{R_c^0}, \quad \hat{k} = \frac{k}{k_c^0}, \quad \hat{q}^2 = \frac{k^2 + \pi^2}{q_c^{0^2}}, \quad \hat{d}^2 = \frac{k^2 + 2\pi^2}{q_c^{0^2}} \ . \quad (2.6e)$$

Here r and $\hat{k}$ are the reduced Rayleigh number and wave number, respectively.

Without the additional modes S and T the model equa-

tions are mathematically identical to the set of equations presented in Ref. 12. However, the physical meaning of the mode variables is a very different one. The authors of Ref. 12 are concerned with *one propagating* set of rolls oriented along the y axis. There the paired modes, e.g., (X_1, X_2) represent real and imaginary part of the complex roll amplitudes. Here, however, X_1, X_2 are the real amplitudes of the *two different standing* roll sets.

C. Convective threshold

Throughout this paper we restrict ourselves to positive separation ratios. Then the conductive state $\mathbf{u}$, θ, $\zeta \equiv 0$ becomes unstable via a stationary instability at

$$r_{\text{stat}}(\hat{k}) = \frac{\hat{q}^6}{\hat{k}^2} \left[1 + \psi + \frac{24}{\pi^2} \frac{\psi \hat{q}^2}{L \hat{k}^2} \right]^{-1} . \tag{2.7}$$

There the critical modes **X**, **Y**, and **U** begin to grow in the linearized model. In fact, the linear properties of our model (2.5) are identical to those of the eight-mode Galerkin model of Ref. 12 since S and T drop out after linearization. The critical wave number of (2.7) vanishes[12] for

$$\psi \geq L[(16/\pi^2) - L]^{-1} .$$

For almost all experimental parameters of MS $(0.01 \leq \psi \leq 0.1, \quad 0.021 \leq L \leq 0.025)$ this condition is fulfilled. However, in all convection patterns observed by MS the wavelength is $\lambda \simeq 2$ so that the wave number $k = \pi$ corresponds to the critical wave number k_c^0 in the reference one-component system at $\psi = 0$. In our free-slip model the reference critical wave number is $k_c^0 = \pi/\sqrt{2}$. Thus we fix $\hat{k} = k/k_c^0 = 1$ in the rest of this paper.

D. Model variables and experimental quantities

Here we give the connection between the model variables and experimentally accessible quantities such as the Nusselt number and shadowgraph pictures. The relation between the fields $\mathbf{u}, \theta, c$ and the model variables is given in Eqs. (2.4) and (2.6).

1. Nusselt number

The laterally averaged vertical heat current density evaluated at the lower boundary, $z = 0$, of the fluid layer is

$$q(z = 0, t) = -\partial_z \langle \theta(\mathbf{x}, t) \rangle \big|_{z=0} + R , \tag{2.8}$$

where $\langle \ \rangle$ abbreviates the lateral average. The conductive heat current density associated with the linear conductive temperature profile is given by the Rayleigh number R. Using (2.8) one finds that the Nusselt number, $N(t) = q(z = 0, t)/R$, is determined in our model by θ_{002},

$$N(t) = \frac{2}{r} Z(t) + 1 . \tag{2.9}$$

2. Shadowgraph pictures

Modulations of the light intensity in shadowgraph pictures are a direct image of the refractive index in the fluid, provided that the amplitudes are small.[19] Assuming small variations of the refractive index to be proportional to small variations $\Delta \rho = \rho - \langle \rho \rangle$ of the density ρ around its mean $\langle \rho \rangle$ the intensity modulation of a shadowgraph picture taken at the top of the fluid layer is a vertically averaged quantity given by

$$\Delta I(x, y, t) = A \int_0^1 dz \, \Delta \rho(x, y, z, t) . \tag{2.10}$$

Here ΔI is the deviation from the mean background light intensity. The proportionality constant A is positive, indicating that positive density fluctuations lead to an increasing refractive index and thus to a greater light intensity. Only the density variation due to the convective temperature and concentration field

$$\rho_{\text{conv}}(x, y, z, t) = -\frac{\kappa \nu}{g d^3} \rho_0 [(1 + \psi)\theta(x, y, z, t) + \zeta(x, y, z, t)] \tag{2.11}$$

enters into (2.11). The conductive part being horizontally homogeneous drops out. Here ρ_0 is the reference density taken, say, at the upper plate.

Within our Galerkin truncation (2.4) ΔI is given by

$$\Delta I(x, y, t) = -A \frac{\kappa \nu}{g d^3} \rho_0 \frac{4\sqrt{2} R_c^0}{q_c^0 \pi}$$
$$\times [p_1(t)\cos(kx) + p_2(t)\cos(ky)] . \tag{2.12a}$$

The two time-dependent prefactors

$$p_i(t) = (1 + \psi)Y_i(t) + U_i(t), \quad i = 1, 2 \tag{2.12b}$$

will be called "shadowgraph pattern amplitudes." Their relative size determines which shadowgraph pattern is observed: p_1 measures the maximal intensity of vertical stripes and p_2 measures the maximal intensity of horizontal stripes. For example, $p_1 = p_2$ corresponds to a square pattern, while $p_2 = 0$ ($p_1 = 0$) corresponds to a striped pattern of parallel convective rolls with axes in the y direction (x direction). In general, the shadowgraph pattern (2.12a) is a superposition of two crossed line patterns.

From the shadowgraph pattern we can deduce information on the structure and spatial phase of the convective flow field. For example, for a striped shadowgraph pattern with $p_2 = 0$ (rolls oriented along the y direction) we have the following chain of implications: dark stripe at $x = 0 \leftrightarrow p_1 > 0 \leftrightarrow$ reduced refractive index $\leftrightarrow$ reduced density $\leftrightarrow$ warm $\leftrightarrow$ upflow, and the opposite for a bright stripe. Note that the implication reduced density $\leftrightarrow$ warm holds only when the convective density variation ρ_{conv} is dominated by θ. In that case the shadowgraph picture is mainly an image of the horizontal variation of the critical mode contribution to the horizontal temperature field. With the exception of the Soret regime shortly above the convective threshold the temperature modes Y are always larger in size than the modes U of the ζ field as we shall see later.

III. CONVECTION IN THE ABSENCE OF IMPERFECTIONS

Here we discuss the results of our model for an ideal-ized situation without symmetry-breaking imperfections such as, e.g., sidewalls that distort amplitudes and favor particular phases of the convective fields or particular patterns. In Sec. IV we shall see that already small inho-mogeneities that simulate in an ad hoc manner the sidewall forcing can give rise to important changes. Since, however, these effects are best understood on the background of the unperturbed model we discuss in this section first the ideal system.

A. Stationary patterns

The stationary convective states are determined by the nontrivial fixed points of the model. There is a set of four equivalent fixed points representing convection in the form of straight rolls (fixed points on the axes of Fig. 2) and another set of four equivalent fixed points describing convection in the form of squares (fixed points on the di-agonals of Fig. 2). The symmetry operations under which the four convective patterns of each set are transformed into each other are: translations by $\lambda/2$ and/or rotations by $\pi/2$.

1. Rolls

In the convective roll states the velocity mode $\hat{u}_{112}$ and the temperature mode $\hat{\theta}_{112}$ are not excited, i.e.,

$$S = 0 = T \tag{3.1a}$$

in the model. Furthermore, for rolls with axes parallel to the y direction,
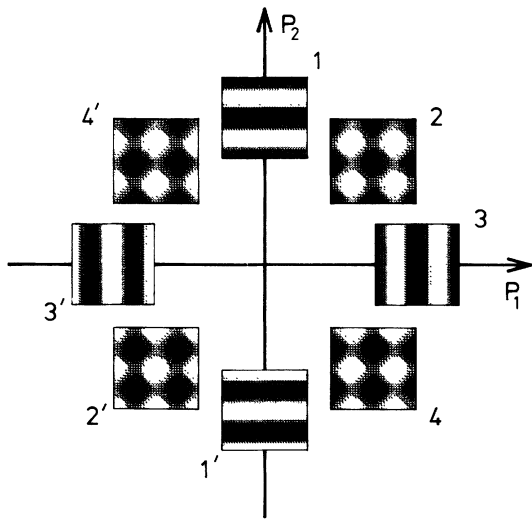

FIG. 2. Convective fixed points of the model projected onto the plane of shadowgraph pattern amplitudes. The correspond-ing patterns are shown in the insets. Therein the light intensity variation (2.12) is shown with ten gray levels. Dark areas indi-cate smaller refractive index implying upflow in the Rayleigh regime.

$$X_2 = Y_2 = U_2 = 0 , \tag{3.1b}$$

so that $p_2 = 0$. There are two fixed points given by[12]

$$Y_1 = rN_1X_1 , \quad U_1 = r\psi \left[\frac{L}{2} - \tfrac{4}{3}X_1^2 \right] N_1\tilde{N}_1X_1 , \tag{3.1c}$$

$$Z = rN_1X_1^2 , \quad V = -r\psi(1+\tfrac{4}{9}L)N_1\tilde{N}_1X_1^2 , \tag{3.1d}$$

$$N_1 = (1+X_1^2)^{-1} , \quad \tilde{N}_1 = (L^2/6+X_1^2)^{-1} . \tag{3.1e}$$

Here X_1^2 is determined by the positive root (for $\psi > 0$ there is only one) of

$$X_1^4 + \alpha X_1^2 + \beta = 0 , \tag{3.1f}$$

with

$$\alpha = 1 + \frac{L^2}{6} - r\left[1 + \psi - \frac{32}{3\pi^2}\psi\right] , \tag{3.1g}$$

$$\beta = -\frac{L^2}{6}(r/r_{\text{stat}} - 1) . \tag{3.1h}$$

The roll-fixed point (3.1) with positive X_1, Y_1, p_1 describes the roll pattern 3 in Fig. 2 with maximal upflow, $\hat{u}_{101}$ positive, at $x = 0$. The other one with negative X_1, Y_1, p_1 has downflow at the origin (pattern 3'). A translation in the x direction by $\lambda/2$ which is equivalent to inverting the rotation direction of each roll transforms the two pat-terns into each other.

The stationary patterns of rolls oriented along the x axis are identical to the above-described ones after a rota-tion by $\pi/2$ in the x-y plane. This corresponds to ex-changing indices 1 and 2 of the mode amplitudes in (3.1). In the plane of the shadowgraph amplitudes the patterns of rolls oriented along the x axis are represented by the fixed points 1 and 1' in Fig. 2.

2. Squares

The convective square patterns correspond to four fixed points of our model for which

$$X_1^2 = X_2^2 , \quad |p_1| = |p_2| , \tag{3.2a}$$

with X_1^2 being the only positive root of the third-order polynomial

$$X_1^6 + a_2X_1^4 + a_1X_1^2 + a_0 = 0 . \tag{3.2b}$$

Here

$$a_0 = \eta \frac{\sigma L^2}{128}(r/r_{\text{stat}} - 1) , \tag{3.2c}$$

$$a_1 = \frac{3}{32}\eta \left\{ \sigma r \left[1 + \psi\left[1 - \frac{32}{3\pi^2}\right]\right] - \sigma\left[1 + \frac{L^2}{6}\right] \right\}$$
$$+ \frac{1}{16}\left[\sigma rL\left[\frac{4\psi}{\pi^2} + \frac{L}{3}(1+\psi)\right] + \tfrac{5}{9}L^2(\tfrac{5}{3}\sigma^2 + 1)\right] , \tag{3.2d}$$

$$a_2 = \sigma r \left[(1+\psi)(\tfrac{1}{4}-\tfrac{3}{16}\sigma) - \frac{4}{3\pi^2}\psi \right] + \tfrac{25}{6}\sigma^2 + \tfrac{1}{12}(5+L^2) \,,$$

$$(3.2e)$$

where

$$\eta = \sigma[r(1+\psi) - \tfrac{500}{27}] \,. \tag{3.2f}$$

For this square convective state the other modes are related to $\mathbf{X} = (X_1, X_2)$ as follows:

$$\mathbf{Y} = r\frac{1+4X_1^2/(3\eta)}{1+[2-25\sigma b/(9\eta)]X_1^2}\mathbf{X}, \quad \mathbf{U} = \psi\frac{L/2 - 8X_1^2/3}{L^2/6 + 2X_1^2}\mathbf{Y} \,,$$

$$(3.2g)$$

$$Z = \mathbf{X} \cdot \mathbf{Y}, \quad V = -\frac{2}{L}(\tfrac{4}{3}\psi\mathbf{Y} + \mathbf{U}) \cdot \mathbf{X} \,, \tag{3.2h}$$

$$S = \frac{\mathrm{sgn}(X_1 X_2)}{\eta}\left[\tfrac{40}{9}X_1^2 + \frac{\sigma b(1+\psi)}{4}\mathbf{X}\cdot\mathbf{Y}\right] \,, \tag{3.2i}$$

$$T = \frac{\mathrm{sgn}(X_1 X_2)}{\eta}\left[\tfrac{4}{3}rX_1^2 + \frac{25\sigma b}{18}\mathbf{X}\cdot\mathbf{Y}\right] \,. \tag{3.2j}$$

The mode vectors $\mathbf{X}$, $\mathbf{Y}$, and $\mathbf{U}$ are collinear and $\mathbf{X}$ and $\mathbf{Y}$ are parallel. Thus the fixed point with $X_1 = X_2$ being positive lies (at least in the Rayleigh regime) in the first quadrant of the p_1-p_2 plane of Fig. 2 giving rise to pattern 2 shown there for $p_1 = p_2 > 0$. One obtains the other square-fixed points, e.g., 4, by rotating the vectors $\mathbf{X}, \mathbf{Y}, \mathbf{U}$ by $\pi/2$ and by changing the sign of S and T. The modes Z and V do not change. One should keep in mind that with $S(\hat{u}_{112})$ and $T(\hat{\theta}_{112})$ being nonzero the fields of vertical velocity and temperature contain contributions $\sim \cos(kx)\cos(ky)$ which are not visible in the shadowgraph intensity distribution because of its lateral dependence $\sin 2\pi z$ that is integrated out in (2.10).

It is interesting and for the discussion in Sec. IV helpful to note that our model without the modes S, T would have a continuous family of fixed points with $\mathbf{X}, \mathbf{Y}, \mathbf{U}$ also being collinear but with an arbitrary common phase angle, e.g., in the X_1-X_2 plane (cf. the discussion in Ref. 12). Projected onto the p_1-p_2 plane these fixed points would form a circle that may be viewed as the bottom of a "Mexican hat" potential. The continuous degeneracy of this "hat" is lifted by including the modes S, T that are excited by the nonlinear coupling, e.g., $(\mathbf{u}\cdot\nabla)\theta$, of critical modes. The effect is to distort the hat vertically in such a way that its groove develops four local minima—the roll states—on the p_1, p_2 axes and in between them four local maxima—the square states—on the diagonals. The hat is also deformed radially with square- and roll-fixed points no longer lying on a circle.

We should like to point out, however, that the Galerkin model equations are not derivable from a potential. We use the picture of the Mexican hat potential only as a convenient means for the discussion.

3. Nusselt numbers

In Fig. 3(a) we show the Nusselt numbers for stationary convection in the form of rolls (thick curve) and squares (dashed line) as a function of reduced Rayleigh number. In the Rayleigh regime, $r \gtrsim 1$, heat is more effectively transported by rolls than by squares. Moreover, shortly above $r = 1$, the slope of the Nusselt number for rolls is close to 2, i.e., the value for a one-component fluid subject to free-slip horizontal boundary conditions.

In the Soret regime $r_{\mathrm{stat}} \leq r \lesssim 1$, on the other hand, convective heat transport is extremely small for both patterns. The convective states bifurcate out of the conductive state at r_{stat} (cf. arrow in Fig. 3) albeit with such a small slope of N that the bifurcation threshold is not visible in Fig. 3(a).

In Fig. 3(b) we show the strengths of the critical θ and ζ modes for the roll pattern of Fig. 3(a). For the square pattern the situation is similar. That θ dominates the buoyancy force (2.11) in the Rayleigh regime ($r > 1$) while ζ dominates in the Soret regime ($r_{\mathrm{stat}} \leq r < 1$) supports the picture of MS that convection is driven in the former mainly by temperature gradients and in the latter mainly by concentration gradients.

4. Stability

The stability of the two above-described stationary convective states was determined by numerically evaluating the eigenvalues of the 10×10 matrix that results after
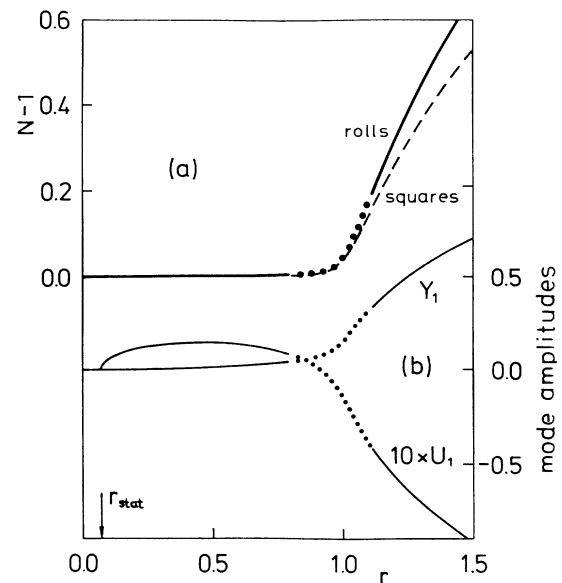

FIG. 3. Nusselt number (a) and selected model amplitudes (b) vs Rayleigh number r for stationary states in the absence of imperfections. Arrow labeled r_{stat} marks the convective threshold. Convective squares are always unstable, however, only very slightly in the range $r < 1$. Rolls are unstable in an interval close to $r = 1$ as indicated by the dots. (b) shows the mode U of the ζ field and the mode Y of the θ field for convective rolls. The former (latter) dominates in the Soret regime, $r < 1$ (Rayleigh regime, $r > 1$). For squares the situation is similar. Parameters are $\psi = 0.1$, $\sigma = 23$, $L = 0.018$.

linearizing the model equations (2.5) around the fixed points (3.1) and (3.2), respectively.

In the Rayleigh regime well above $r = 1$ squares are strongly unstable with large positive eigenvalues, while rolls are quite stable there with the largest real part being sufficiently negative. As an aside we mention that without the S, T modes the resulting rotational symmetry of the aforementioned undistorted Mexican hat potential would lead to a zero eigenvalue for the roll- and the square-fixed points.

In the Soret regime, $r \lesssim 1$, on the other hand, rolls are very weakly stable and squares are very weakly unstable. In each case there is one real eigenvalue very close to zero. For example, for the parameters of Fig. 3 this eigenvalue is $\gamma_{rolls} = -2.5 \times 10^{-5}$ and $\gamma_{squares} = 2.5 \times 10^{-5}$ at $r = 0.5$. For the potential picture of the Mexican hat this implies that the deformation by the S, T modes is very small: the roll minima are very shallow and the square maxima are very small in the Soret regime. Consequently, there is in the ideal system an extremely slow approach on a time scale $\sim 1/\gamma_{rolls}$ to a final roll state, whereas in the experiments of MS the square state was stable in the Soret regime (cf. Sec. IV for a discussion of the stabilization of squares by symmetry-breaking imperfections).

An important feature for understanding the convective behavior upon increasing the Rayleigh number towards $r \simeq 1$ is the Hopf bifurcation dynamics there: In the Soret regime there are for both, the square- as well as for the roll-fixed point, two complex-conjugate eigenvalues with a small negative real part. With increasing r this real part grows, becomes positive at a threshold value ($r = 0.78$ in Fig. 3), and causes a Hopf bifurcation into a limit cycle there.

B. Oscillating patterns

For Rayleigh numbers around $r = 1$ between the Soret regime and the Rayleigh regime (dotted region in Fig. 3) no stable stationary convective solution exists. There we have found limit cycles numerically. The projection of their trajectories onto the p_1-p_2 plane has typically an ellipsoidal shape centered around the origin $p_1 = p_2 = 0$. Depending on r, however, the ellipses can also degenerate to a straight line through the origin. We found these "squeezed" forms typically for $r < 1$ when all amplitudes were small. These linelike trajectories, e.g., between 1 and 1' in Fig. 2, correspond to patterns that periodically decay to zero and grow again with globally reversed flow directions. The Nusselt number periodically goes to zero when the flow reverses its direction.

On the other hand, circular-shaped limit cycle trajectories were typically found for $r > 1$ when the convective amplitudes were appreciable. This type of limit cycle represents an alternating sequence of convective square and roll patterns in which each of the eight patterns of Fig. 2 is successively appearing along the circular orbit running, e.g., through the points 1-2-3-4-1'-2'-3'-4' in the p_1-p_2 plane. In the X_1-X_2 plane the trajectory is not purely circular since the Mexican hat is deformed in radi-

al direction by the S, T modes. Therefore $|\mathbf{X}(t)|$ and with it $Z(t)$ and also the Nusselt number $N(t)$ oscillate weakly around a mean that is smaller than the Nusselt number of the unstable stationary convective rolls. Furthermore, the limit cycle remains stable for r much larger than the value where the roll-fixed point (cf. Fig. 3) becomes stable again. Eventually the ideal model system undergoes a hysteretic transition to the stable roll-fixed point.

Although the alternating patterns and the oscillations in heat transport are somewhat similar to the results of MS, this limit cycle is not the experimentally observed one. One reason is the oscillation frequency which in the ideal system grows with r, while it decreases with r in the experiment of MS and of Le Gal et al.[11] The other reason is the way square and roll patterns alternate as described below.

IV. EFFECT OF SIDEWALLS

A. Sidewall forcing in the experimental square cell

Here we argue that in the experimental cell of MS with a square-shaped horizontal cross section there are sidewall forces that favor particular patterns, i.e., certain phase relations of the patterns relative to the sidewalls.

Let us first recall the limit cycles of the ideal model system without sidewalls: In each case the sequence of patterns is such that the convective flow periodically reverts its direction, since with a particular pattern n also its inverse n' is part of the cycle. Take as an example the circular trajectory 1-2-3-4-1'-2'-3'-4' in the p_1-p_2 plane of Fig. 2. Thus roll states 1 and 1' with reversed rotation directions of the rolls periodically appear.

The experimental shadowgraph pictures [Figs. 4(c)–4(e) of MS covering half a period], on the other hand, clearly show that patterns with globally reversed flow directions do not appear. This is most easily seen from the fact that there are places (lying on a square lattice) that remain always black, e.g., close to the sidewalls, while others remain always bright. Furthermore, the number of horizontal and vertical lines of black dots or black stripes remains fixed at 12 and also the number of bright vertical and horizontal stripes, 11, does not change. This also implies that the turning directions of the rolls remain the same. For opposite turning directions one would have 11 black and 12 bright stripes given that the number of rolls—22 in the x and y directions—does not change.

The shadowgraphs of MS strongly suggest that the limit cycle in the experimental cell consists of a sequence of patterns, say, 1-2-3-2-1. . . of Fig. 2, such that there are always black dots or a black stripe near the sidewalls. Starting from point 1 in this cycle the flow intensity of a fixed set of 22 convective rolls with axes parallel to x decreases, while simultaneously a similar fixed set of 22 rolls with axes in the y direction grows. When the intensities of the x and y rolls are equal we have a square pattern (point 2). Then the intensity of the x rolls decreases and that of the y rolls reaches its maximum (point 3). In the second half of the cycle x rolls grow again and y rolls

decrease and the system returns to point 1.

Note that in this cycle the local flow direction remains unchanged everywhere. In comparison with the symmetry of the unbounded ideal system under reversing the turning direction of rolls or of replacing upflow by downflow the experimental limit cycle implies that the experimental setup favors a particular phase of the flow field, e.g., a particular rotation direction of a particular roll. For a fixed number of rolls or squares this is a manifestation of sidewall forcing that leads to a particular flow configuration near the wall.

B. Incorporating symmetry-breaking forces into the model

Since our model assumes a fluid layer extended laterally to infinity it does not contain symmetry-breaking sidewall forces that favor particular phases of the flow patterns. We tried to incorporate the effect of these imperfections by adding, in a purely phenomenological and ad hoc manner, small inhomogeneities, i.e., small generalized forces to the equations of motions of the pattern-carrying modes. Doing so we were guided by the approach of Ahlers et al.,[16] who incorporated the sidewall forces[20] caused by temperature modulation into a Lorenz model. We found good agreement with experiment for forces ξ that couple to the ζ field being a combination of concentration and temperature.

In the rest of this paper we present results of our modified Galerkin model where Eq. (2.5c) is replaced by

$$\tau \dot{\mathbf{U}} = -\frac{L}{3}\mathbf{U} + \psi\mathbf{Y} + V\mathbf{X} + \xi , \qquad (4.1)$$

with a constant inhomogeneity ξ. Here we have used $\hat{k} = \hat{q} = 1$ as in the rest of this paper.

For the square convection cell used by MS the forcing caused by each of the sidewalls should be the same which implies $\xi_1 = \xi_2$ in our model. For a rectangular cell, on the other hand, $\xi_1/\xi_2 \neq 1$ would be a function of the ratio of the side lengths. In the picture of the Mexican hat potential the forcing ξ with $\xi_1 = \xi_2 > 0$ tilts the hat along the 135° diagonal axis, thereby lowering its groove in the first quadrant. Hence the square pattern 2 and the adjacent roll patterns 1 and 3 (notation of Fig. 2) become favored. For a rectangular-shaped cell, say, with side lengths $L_y \ll L_x$, one would have $\xi_2 \simeq 0$ and $\xi_1 \neq 0$, thereby favoring the roll patterns 3 or 3'. It is interesting to note that MS found well-developed regular square patterns only in square-shaped convection cells, i.e., in systems for which in our model the forces $\xi_1 = \xi_2$ provide the largest bias for squares.

C. Results

1. Stationary convection

We have numerically evaluated the stationary solutions of our model equations in the presence of a small forcing $\xi_1 = \xi_2 = \xi > 0$ by a Newtonian algorithm. Their stability was determined by solving the associated 10×10 eigenvalue problem as described in Sec. III.

In agreement with experiments we found that in the

Rayleigh regime, well above $r = 1$ only stationary convective rolls are stable. The threshold Rayleigh number r_2 (cf. Fig. 4) down to which they are stable depends slightly on the size of ξ. But otherwise the small inhomogeneity ξ alters the stationary roll-fixed points only insofar as fixed points 1 and 3 are slightly favored over 1' and 3'. Thus in the far Rayleigh regime the internally generated forces due to nonlinear mode interactions dominate over the external forcing ξ and determine the fixed point behavior of the system.

In the Soret regime, however, squares being slightly unstable in the ideal system are stabilized by the sidewall forcing, while rolls are destabilized. The reason is that in the Soret regime the mode amplitudes are so small and the Mexican hat potential is so shallow that already a small inhomogeneity—a small tilt of the "potential"—stabilizes pattern 2 and destabilizes the others.

At $r = r_1$ (Fig. 4) this stationary convective square pattern becomes unstable as the system undergoes a forwards Hopf bifurcation into an oscillatory convective state. We have chosen $\xi = 0.005$ such that the Hopf bifurcation at r_1 coincides with the experimental onset of oscillations in the large square cell of MS.

2. Oscillating patterns

In the range of Rayleigh numbers between r_1 and r_2 (Fig. 4) stationary roll and square convection is unstable. Instead our perturbed model has stable limit cycle solutions which we have determined numerically. Their time behavior differing significantly from that of the ideal unforced system will be discussed further below.

The associated time-averaged Nusselt number is shown in Fig. 4 by dots in comparison with the experimental results (open circles) for the oscillatory states as far as we could read them off the figures published by MS. The existence range of oscillatory patterns in the experimental cell seems to be smaller than in our model. This might be
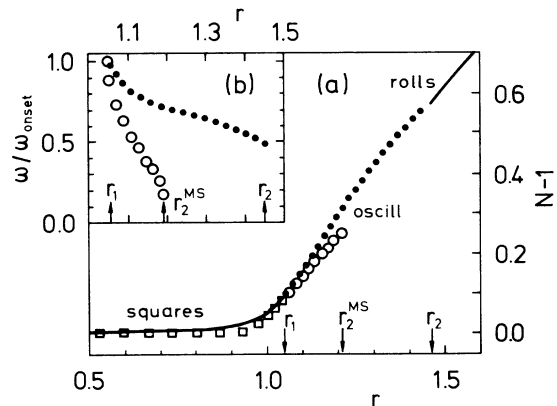
FIG. 4. Mean Nusselt number and reduced oscillation frequency (inset) vs reduced Rayleigh number. Solid lines (stationary convection) and dots (oscillatory convection) result from our model with forcing $\zeta = 0.005$ for $\psi = 0.1$, $L = 0.018$, $\sigma = 23$. Open squares and circles are experimental results of MS for stationary square convection and oscillatory convection, respectively. Oscillations first appear at r_1, stationary rolls at r_2.

due to our crude and presumably not fully adequate incorporation of the sidewall forcing effect. Furthermore, our model uses free-slip boundaries, whereas the no-slip experimental boundaries might slow down the periodically alternating growth of the two orthogonal sets of convection rolls appearing in the cycle. A hint in this direction is the fact that at the threshold $r = r_1$ the experimental oscillation period ($\simeq 2.8 d^2/\kappa$) is about a factor of 10 longer than that of our free-slip model.

We have therefore plotted in the inset of Fig. 4 the oscillation frequencies reduced by their respective values at onset, $r = r_1$. With growing Rayleigh number the frequency decreases towards a finite value at $r = r_2$ where the roll solution becomes stable again. Our model shows in the immediate vicinity of r_2 a hysteretic transition to stationary roll convection.

In Fig. 5 we show the trajectories of the limit cycles projected onto the plane of the pattern amplitudes p_1, p_2 which determine the light intensity distribution of the shadowgraph pictures. This limit cycle where the three shown patterns appear successively strongly resembles the experimentally observed pattern sequence.

In the lower half of Fig. 6 we show for the limit cycle at $r = 1.3$ and 1.05 one period of the shadowgraph amplitude $p_1(t)$ starting from the positions marked in Fig. 5 by the arrows. For r close to r_1 the oscillations are almost sinusoidal. In agreement with experiment they become more anharmonic with increasing r and plateaus begin to form. The amplitude $p_2(t)$ is phase shifted relative to $p_1(t)$ by half a period. According to (2.12a) the light intensity at a position x,y is the superposition of $p_1(t)$ and $p_2(t)$ weighted by $\cos(kx)$ and $\cos(ky)$, respectively. Since for arbitrary x,y these two contributions can add up to almost arbitrary curves one has to be careful in interpreting light intensity curves measured at an arbitrary position.

In the upper half of Fig. 6 we show the Nusselt number oscillating with twice the frequency of the pattern oscillation. The reason is the mirror symmetry of Fig. 5 at the
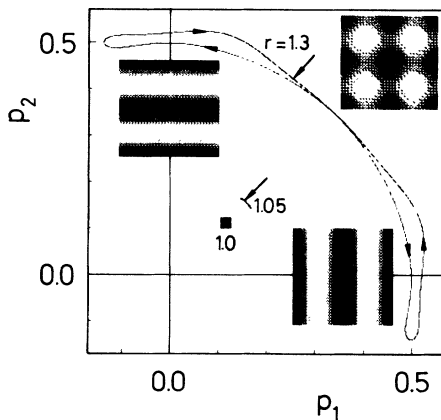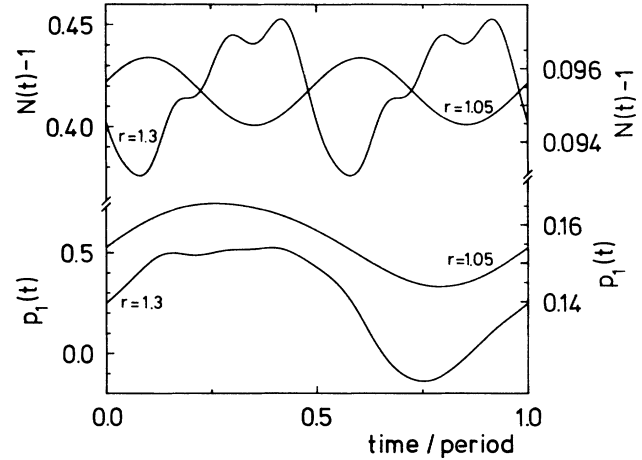

FIG. 6. Shadowgraph pattern amplitude p_1 and Nusselt number N for one period of the limit cycle at $r = 1.3$ (left ordinate), and $r = 1.05$ (right ordinate) shown in Fig. 5 (start is marked there by the respective arrow). The other amplitude p_2 entering into the shadowgraph light intensity $\Delta I(x,y,t)$ (2.12a) is phase shifted relative to p_1 by half a period. See text for details and a discussion of the double frequency oscillation of $N(t)$. Parameters as in Fig. 4.

$45°$ diagonal resulting from our choice of $\xi_1 = \xi_2$. This lets the two convective roll patterns occurring in the cycles of Fig. 5 be identical up to a rotation by $\pi/2$. In an experimental square cell, on the other hand, one might expect imperfections to be present that favor one roll direction, say x, over the other one, leading eventually to different Nusselt numbers for the x- and y-roll states. In such an experimental situation the periodicity of $N(t)$ with half the pattern period would no longer hold exactly but only approximately so. In fact, MS state that the Nusselt number oscillates with twice the frequency of the cycle.

In view of the above discussion a careful analysis of the period of $N(t)$ in comparison with that of the convective patterns might provide a sensitive tool to measure the imperfections of a square cell used in convection experiments.

V. SUMMARY AND CONCLUSION

We have derived an extended and generalized Lorenz model for binary mixtures at positive separation ratios subject to stress-free, impermeable horizontal boundaries. In agreement with experiments the model shows that convection sets in at a Rayleigh number r that is considerably reduced in comparison to the critical one, $r = 1$, in a one-component fluid, in particular if $\psi/L \gg 1$. In the Soret regime just above onset the buoyancy force driving the convective flow is dominated by the concentration field but the convective heat transport and the slope of the Nusselt number N are extremely small. In the Rayleigh regime at $r > 1$ temperature modes dominate the buoyancy force and N grows as in a one-component fluid.

In the absence of symmetry-breaking inhomogeneities the model equations have a set of four equivalent fixed

FIG. 5. Limit cycle trajectories projected onto the p_1-p_2 plane of shadowgraph pattern amplitudes. The closed square represents the stationary square convective state at $r = 1$. Parameters as in Fig. 4.

points representing stationary convection in the form of straight rolls and a set of four equivalent fixed points describing convection in the form of squares. Two of the former represent rolls oriented along the x direction which transform into each other by translating the pattern in the y direction by half a wavelength or, equivalently, by reverting everywhere the flow direction. Similarly there are two stationary states for rolls oriented along the y direction. The four square patterns are related to each other by translations by $\lambda/2$ along x and/or y.

In the idealized system square (roll) convection is very weakly unstable (stable) in the Soret regime, while rolls (squares) are strongly stable (unstable) in the far Rayleigh regime. In a region of r values between these two regimes there is no stable stationary convective state. There a stable limit cycle solution exists with alternating rolls and squares such that every pattern out of the two sets of symmetry-degenerated states appears. Thereby the local flow direction periodically reverses. In the experimental cell of MS, however, only patterns with certain phase relations (upflow and downflow positions) relative to the sidewalls are realized: with a fixed number of rolls or squares in the square-shaped container the local flow direction of the rolls or squares never changes—only the amplitudes vary.

To incorporate the sidewall forces selecting the phase of the pattern we introduced into the Galerkin model, in a purely phenomenological way, a small inhomogeneous forcing term that favors a particular phase of the roll or square pattern, say, one with upflow at the origin $x = y = 0$. Within the picture of a deformed Mexican hat potential accommodating the symmetry-degenerated

square- and roll-fixed points the forcing would tilt the hat slightly towards the favored patterns (the hat serves only as a convenient means for discussion—the Galerkin equations are not derivable from a potential).

In the far Rayleigh regime the inhomogeneity does not change the stationary roll solution that results from large internally generated forces due to nonlinear mode interactions. In the Soret regime, however, where the mode amplitudes are small the sidewall forcing stabilizes squares and makes rolls unstable there. Tilting the hat also changes the limit cycle in the intermediate regime around $r = 1$. Instead of running through all eight patterns along the "groove of the hat" the system now oscillates as in the experiments between two specific patterns of rolls along x and y with one square pattern in between such that the local flow direction does not change.

With increasing r the oscillation frequency decreases from its value at the Hopf bifurcation out of the stationary square solution towards a final finite value when the limit cycle undergoes at larger r a transition with small hysteresis into a stationary roll state. The form of the oscillations becomes more and more anharmonic. The Nusselt number oscillates with precisely half the period of the pattern cycle if the states with rolls along the x and y directions are identical.

ACKNOWLEDGMENTS

[1]For a review see, for instance, J. K. Platten and J. C. Legros, *Convection in Liquids* (Springer, Berlin, 1984).

[2]G. Ahlers and I. Rehberg, Phys. Rev. Lett. **56**, 1373 (1986).

[3]P. Kolodner, A. Passner, C. M. Surko, and R. W. Walden, Phys. Rev. Lett. **56**, 2621 (1986).

[4]C. M. Surko and P. Kolodner, Phys. Rev. Lett. **58**, 2055 (1987).

[5]E. Moses and V. Steinberg, Phys. Rev. A **34**, 693 (1986); **35**, 1444(E) (1987).

[6]E. Moses and V. Steinberg, Phys. Rev. Lett. **57**, 2018 (1986); V. Steinberg and E. Moses, in *Patterns, Defects, and Micro-Structures in Nonequilibrium Systems*, NATO Advanced Study Institute, E-121, edited by D. Walgraef (Martinus Nijhoff, Amsterdam, 1987).

[7]R. Heinrichs, G. Ahlers, and D. S. Cannell, Phys. Rev. A **35**, 2761 (1987).

[8]D. T. J. Hurle and E. Jakeman, J. Fluid Mech. **47**, 667 (1971).

[9]H. Brand, P. C. Hohenberg, and V. Steinberg, Phys. Rev. A **30**, 2548 (1984).

[10]G. Z. Gershuni and E. M. Zhukhovitskii, *Convective Stability of Incompressible Fluids* (Keter, Jerusalem, 1976); L. D. Landau and E. M. Lifshitz, *Fluid Mechanics* (Pergamon, New York, 1959).

[11]P. Le Gal, A. Pocheau, and V. Croquette, Phys. Rev. Lett. **54**, 2501 (1985).

[12]S. J. Linz and M. Lücke, Phys. Rev. A **35**, 3997 (1987); **36**, 2486(E) (1987); in Propagation in Nonequilibrium Systems, edited by J. E. Wesfreid, H. R. Brand, P. Manneville, G. Albinet, and N. Boccara [Springer Proceedings in Physics, Vol. 30 (1988)].

[13]M. C. Cross and K. Kim, Phys. Rev. A **37**, 3909 (1988).

[14]E. Knobloch and D. R. Moore, Phys. Rev. A **37**, 860 (1988).

[15]S. J. Linz, M. Lücke, H. W. Müller, and J. Niederländer (unpublished).

[16]G. Ahlers, P. C. Hohenberg, and M. Lücke, Phys. Rev. A **32**, 3493 (1985).

[17]J. Niederländer, diploma thesis, Universität Saarbrücken, 1986.

[18]See, e.g., G. Veronis, J. Mar. Res. **23**, 1 (1965); J. K. Platten and G. Chavepeyer, Int. J. Heat Mass Transfer **18**, 1071 (1975); M. G. Velarde and J. C. Antoranz, Phys. Lett. **72A**, 123 (1979); L. N. da Costa, E. Knobloch, and N. O. Weiss, J. Fluid Mech. **109**, 25 (1981); a similar truncation for a one-component fluid was introduced earlier by E. N. Lorenz, J. Atmos. Sci. **20**, 130 (1963).

[19]V. Steinberg, G. Ahlers, and D. S. Cannell, Phys. Scr. **32**, 534 (1985).

[20]M. C. Cross, P. C. Hohenberg, and M. Lücke, J. Fluid Mech. **136**, 269 (1983).
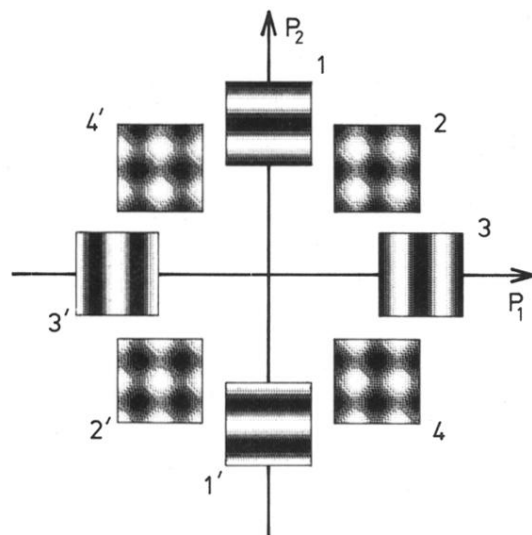
FIG. 2. Convective fixed points of the model projected onto the plane of shadowgraph pattern amplitudes. The corresponding patterns are shown in the insets. Therein the light intensity variation (2.12) is shown with ten gray levels. Dark areas indicate smaller refractive index implying upflow in the Rayleigh regime.
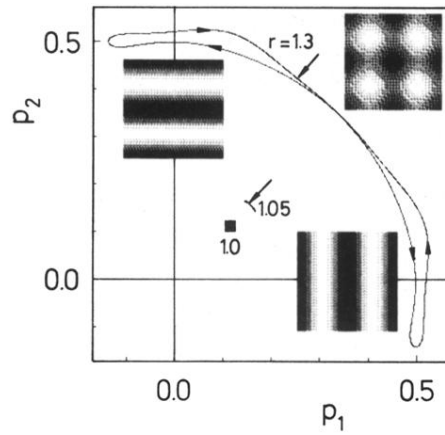
FIG. 5. Limit cycle trajectories projected onto the p_1-p_2 plane of shadowgraph pattern amplitudes. The closed square represents the stationary square convective state at $r = 1$. Parameters as in Fig. 4.